Supporting Information

Energy-Filtering and Anisotropic Structural Response in Polyaniline:CSA Hybrids for Flexible Thermoelectrics

Anmol Sharma[1,2], Nagendra Singh Chauhan[1*], and Takao Mori[1,2*]

[1]Center for Materials Nanoarchitectonics (WPI-MANA), National Institute for Materials Science (NIMS), Namiki 1-1, Tsukuba, 305-0044, Japan.
[2]Graduate School of Pure and Applied Sciences, University of Tsukuba, 1-1-1 Tennodai, Tsukuba, Ibaraki 305-8573, Japan.

[*]CHAUHAN.NagendraSingh@nims.go.jp, MORI.Takao@nims.go.jp

S1. Synthesis and Experimental Details.

S1.1. Synthesis. High-purity raw materials from Sigma-Aldrich company were weighed in accordance to the nominal composition $Mg_{0.99}Cu_{0.01}Ag_{0.97}Sb_{0.99}$ employing high-energy ball milling process. [1] Polyaniline (emeraldine base, average M_w >100000, Sigma Aldrich), *m*-cresol ($CH_3C_6H_4OH$, 99%, Sigma Aldrich), camphor sulfonic acid (CSA, $C_{10}H_{16}O_4S$, 99%, Sigma Aldrich) and Ethanol (C_2H_5OH, 98%, Wako chemicals) were used as received, without any additional purification.

S1.2. Synthesis of PANI:CSA/MACS flexible films. The synthesis of $Mg_{0.99}Cu_{0.01}Ag_{0.97}Sb_{0.99}$ powder were performed as previously reported (Details in Methods).[1] Flexible PANI/MACS composite films were fabricated through a solution-processing route optimized for homogeneous dispersion and robust polymer–filler integration. The emeraldine salt form of polyaniline (PANI:CSA) was first prepared by protonating PANI in its emeraldine base (EB) state with camphorsulfonic acid (CSA) in a 1:0.5 molar ratio. The mixture was manually ground in an agate mortar for 10 min to ensure intimate mixing, followed by dissolution in 2.5 mL of *m*-cresol under continuous stirring for ~24 h, yielding a uniformly doped PANI:CSA solution. In parallel, $Mg_{0.99}Cu_{0.01}Ag_{0.97}Sb_{0.99}$ (MACS) powders were dispersed in 1.5 mL of *m*-cresol at varying loadings (20–70 wt.%). Each dispersion underwent sequential stirring and ultrasonication for 1 h to prevent agglomeration and achieve a stable dispersion. The MACS dispersions were subsequently combined with the PANI:CSA/*m*-cresol solution. The mixed suspensions were subjected to three iterative cycles of stirring (10 min) and ultrasonication (10 min), ensuring nanoscale mixing and strong interfacial coupling between the polymer chains and inorganic fillers. A pristine PANI:CSA reference solution was prepared by diluting the PANI:CSA solution with an additional 1.5 mL of *m*-cresol to match the final volume of composite inks.

The resulting inks were drop-cast onto pre-cleaned glass substrates (25 cm × 20 cm) and dried on a hot plate at 40 °C for 24 – 36 h to facilitate slow evaporation of *m*-cresol and prevent structural cracking. The dried, free-standing films were gently delaminated from the substrate by immersion in deionized water, yielding flexible and free-standing PANI/MACS composite films with excellent mechanical integrity. A schematic illustration of the complete fabrication process is provided in **Figure 1**.

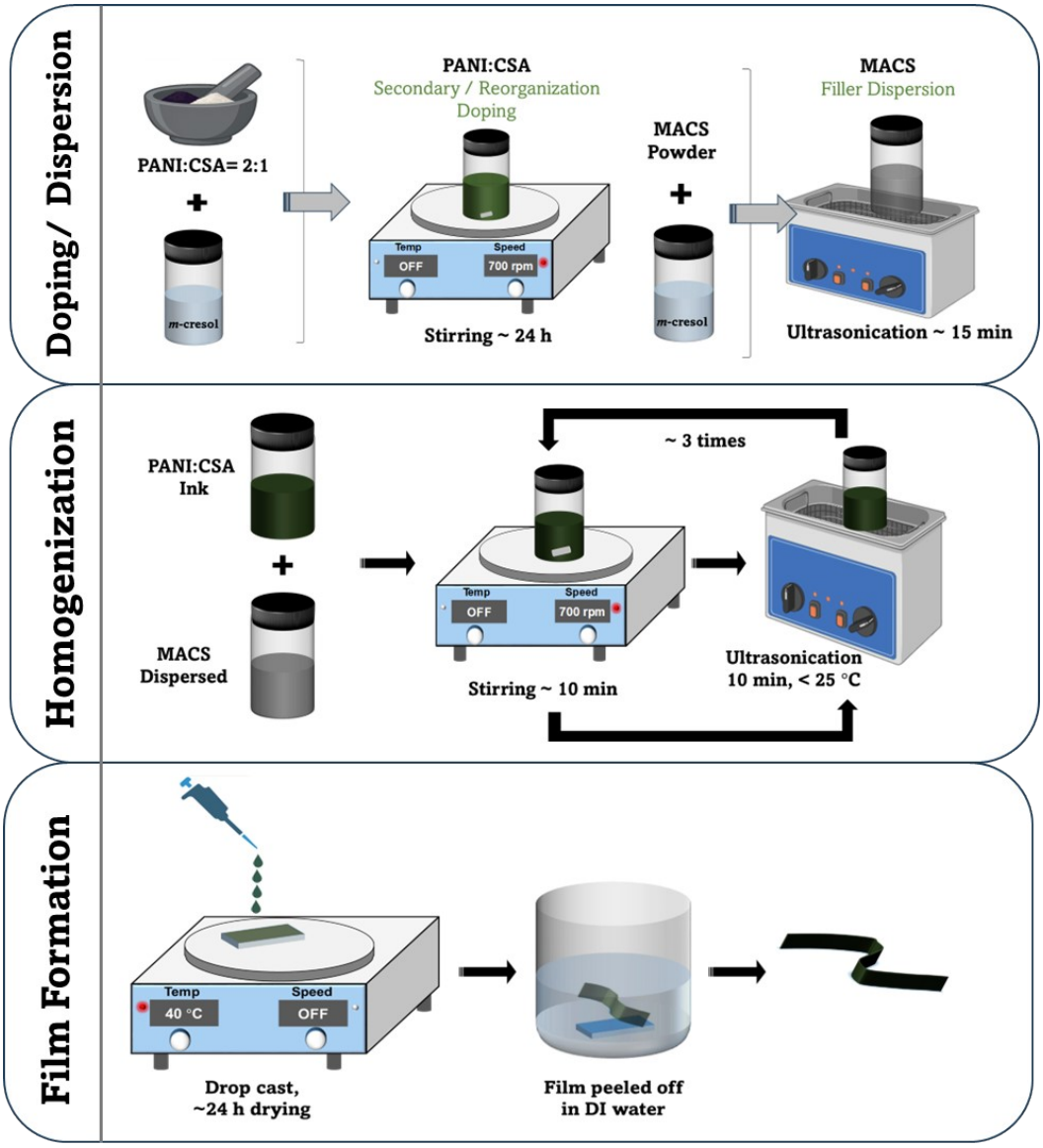

Figure S1. Schematic representing fabrication process of flexible PANI:CSA/MACS nanocomposite free-standing film.

S1.3. Characterization Techniques. The temperature-dependent Seebeck coefficient, S(T), and electrical conductivity, $\sigma(T)$, were measured simultaneously in the temperature interval between 298 and 373 K using the four-probe method (ZEM–3, ADVANCE RIKO, Japan) with a measurement uncertainty of ~ ± 5%. The total thermal conductivity (k) was calculated from the thermal diffusivity (D), specific heat (C_p), and volumetric density measured using the Laser flash technique (LFA 467, Hyperflash, Netzsch, Germany) on the circular disc-shaped samples with a diameter of ~10 mm. The Hall carrier concentration (n_H) and mobility (μ_H) were measured using a ResiTest 8300 Series (Toyo Technica). The X-ray diffractometer (MiniFlex, Rigaku) with CuK_α radiation operating at kV × 15 m was used for obtaining XRD patterns, and the scanning rate was set to 1°/min. The microstructural morphologies and composition of the samples were characterized using a scanning electron microscopy (SEM, FESEM, Hitachi SU8000) equipped with an energy dispersive spectrometer (EDS, XFlash FlatQUAD 5060F). The chemical interaction of film samples was analyzed using a Raman microscope (Renishaw inVia Reflex) using a 785 nm laser and grating of 1200 I/mm with an exposure time of 10 sec. The thickness of the free-standing films was measured using Bruker's surface profiler and confirmed via cross-sectional SEM (FESEM, Hitachi SU8000). The chemical states were analyzed using X-ray photoelectron spectrometer (XPS-QuanteraSXM, ULVAC PHI Inc.), with a source gun type of Al-K_α and source power of ~25 W. The UV–Vis–NIR absorption spectroscopy was performed using UV-Vis-NIR (V-770), JASCO, using an integrating sphere unit in the range of 200 nm – 1000 nm, to investigate the optical transitions and electronic structure of the samples. The output voltage of the FTEG was measured via a digital multimeter.

S2. Structural Refinement Details.

Table S1. Refined *d* Spacing and (*hkl*) indexation based on pseudo-orthorhombic lattice symmetry (Space group: *Pc2a*, 32) of PANI:CSA complex[2] for the synthesized PANI:CSA/ MACS based nanocomposite films.

(*hkl*)	Pouget et al.[2]	This Work						
		PANI:CSA	PANI : CSA/MgAgCuSb Nanocomposite Films					
			20%	30%	40%	50%	60%	70%
(010)	7.88	9.44	13.5	12.28	13.38	11.92	11.30	12.10
(101)	5.87	6.87	7.52	7.33	7.53	7.16	7.01	7.21
(002)	-	6.05	6.33	6.29	6.28	6.10	6.02	6.12
(111)	-	5.60	5.80	5.67	5.80	5.59	5.50	5.62
(012)	4.38	5.13	5.18	5.13	5.14	5.02	4.97	5.04
(020)	-	4.93	4.98	4.81	4.95	4.78	4.70	4.80
(102)	4.18	4.80	4.81	4.80	4.80	4.71	4.67	4.72
(112)	-	4.39	4.22	4.20	4.21	4.14	4.11	4.15
(200)	3.57	4.22	3.94	3.91	3.97	3.89	3.87	3.90
(121)	-	3.96	3.82	3.76	3.81	3.73	3.70	3.74
(201)	-	3.99	3.68	3.67	3.70	3.65	3.63	3.65
(210)	3.24	3.87	3.61	3.57	3.60	3.54	3.52	3.55
(022)	-	3.78	3.58	3.56	3.59	3.53	3.51	3.54

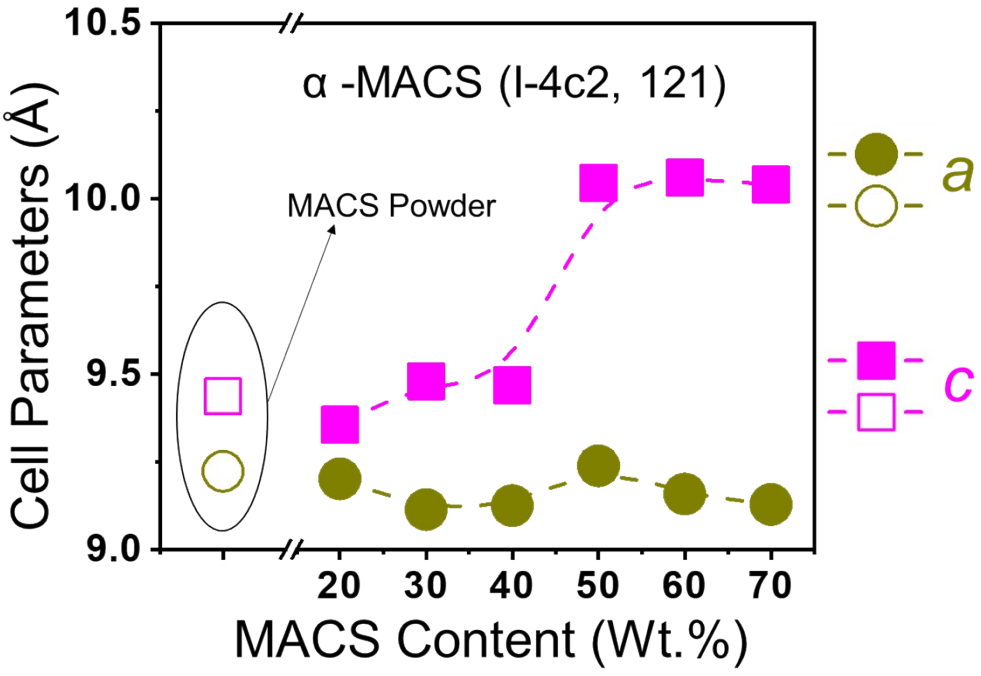

Figure S2. Lattice parameter for unit cell of α-MgAgSb.

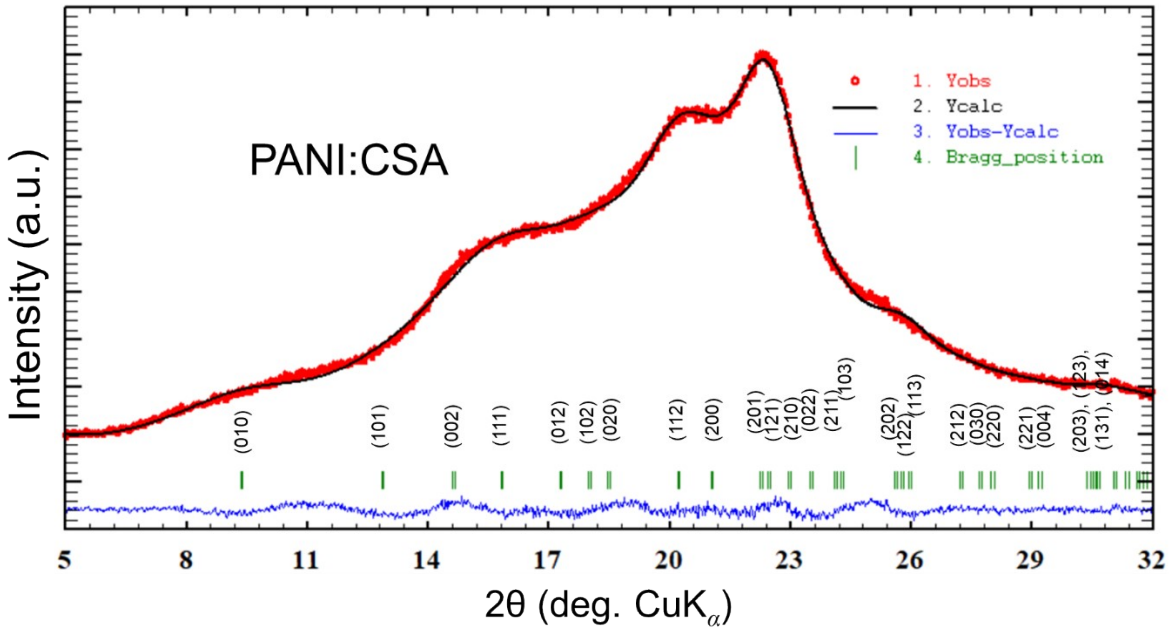

Figure S3. Rietveld refinement of XRD patterns of synthesized PANI:CSA.

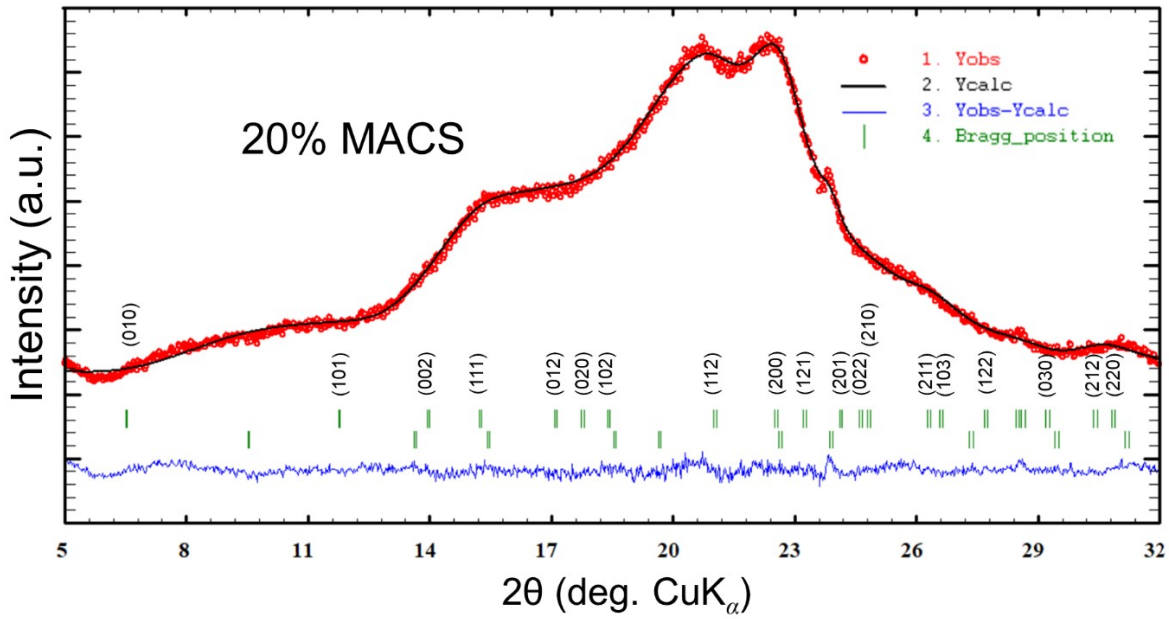

Figure S4. Rietveld refinement of XRD patterns PANI:CSA/MACS ($x \approx 20\%$) nanocomposites.

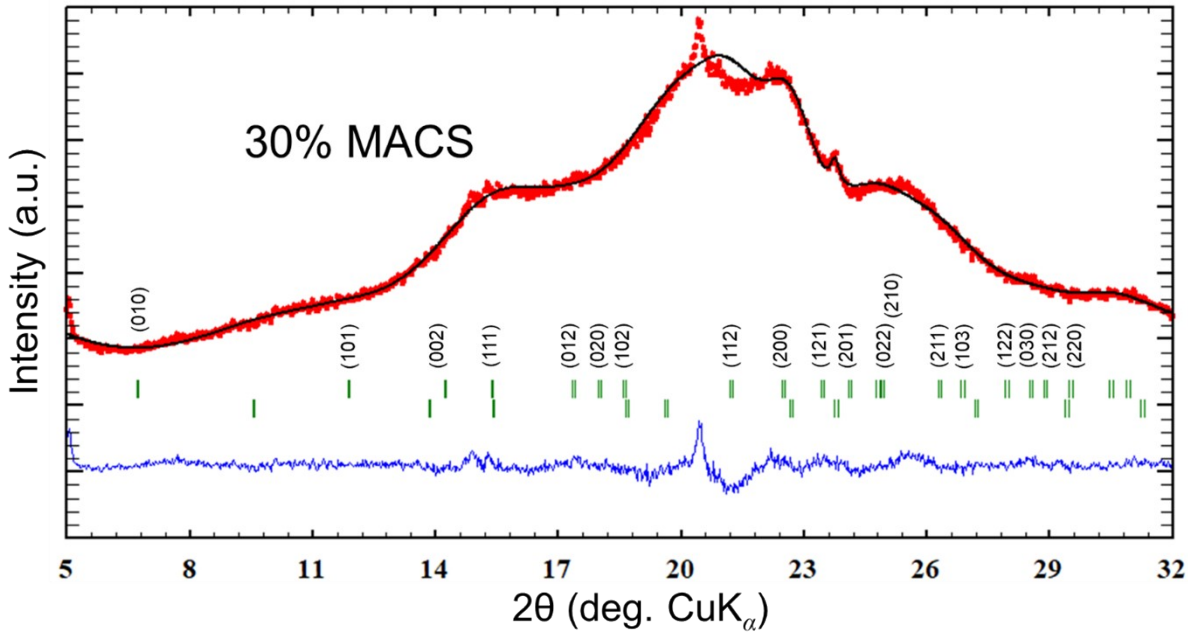

Figure S5. Rietveld refinement of XRD patterns PANI:CSA/MACS ($x \approx 30\%$) nanocomposites.

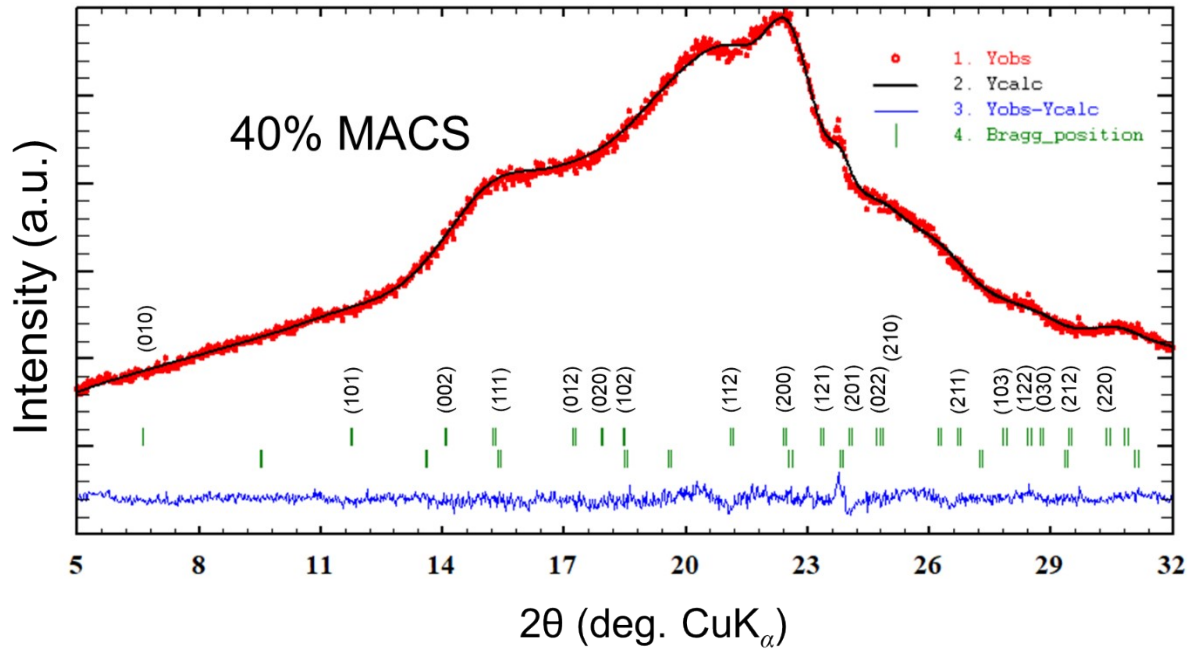

Figure S6. Rietveld refinement of XRD patterns PANI:CSA/MACS ($x \approx 40\%$) nanocomposites.

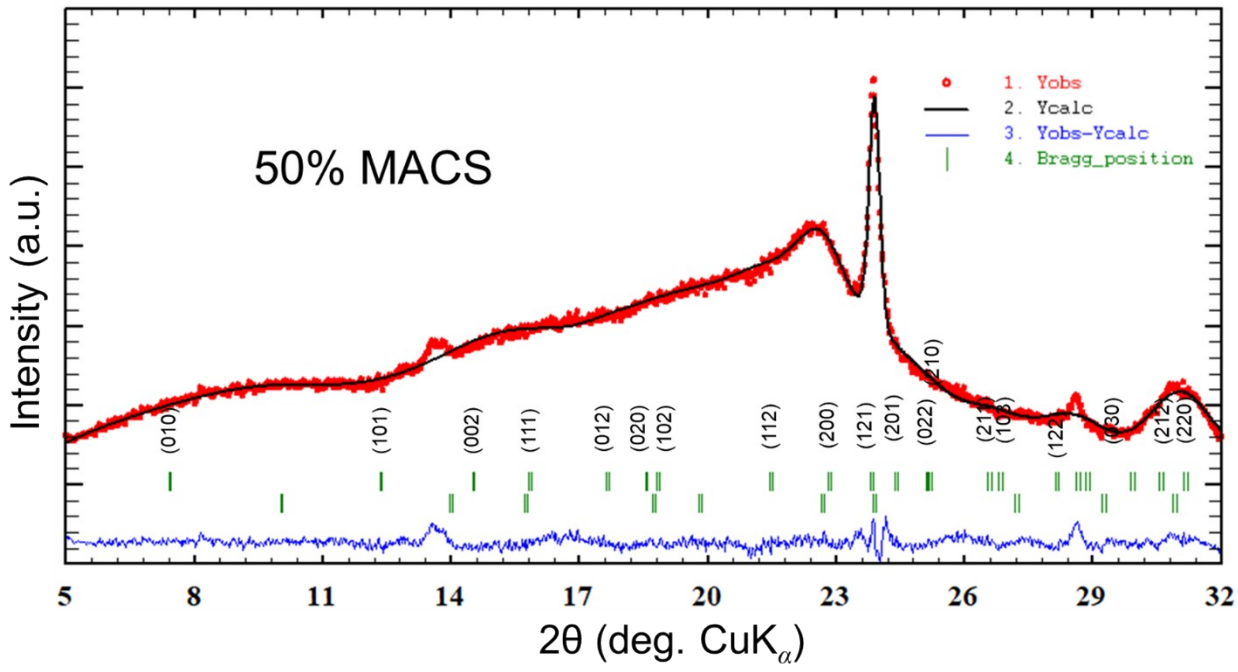

Figure S7. Rietveld refinement of XRD patterns PANI:CSA/MACS ($x \approx 50\%$) nanocomposites.

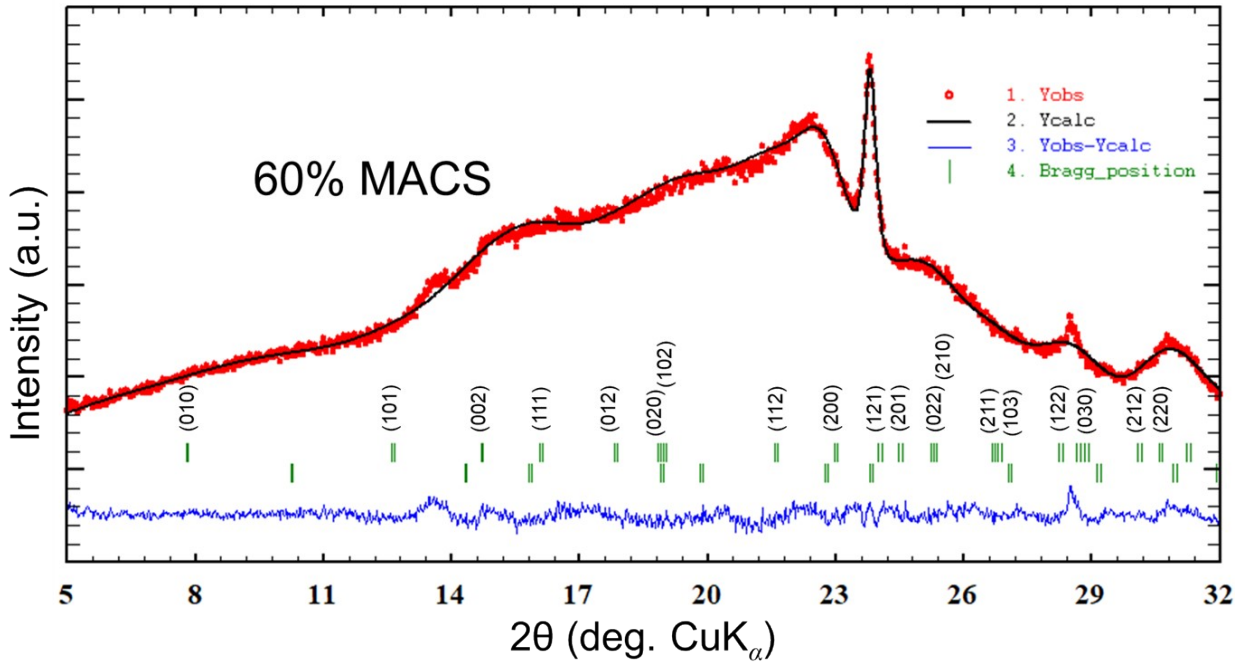

Figure S8. Rietveld refinement of XRD patterns PANI:CSA/MACS ($x \approx 60\%$) nanocomposites.

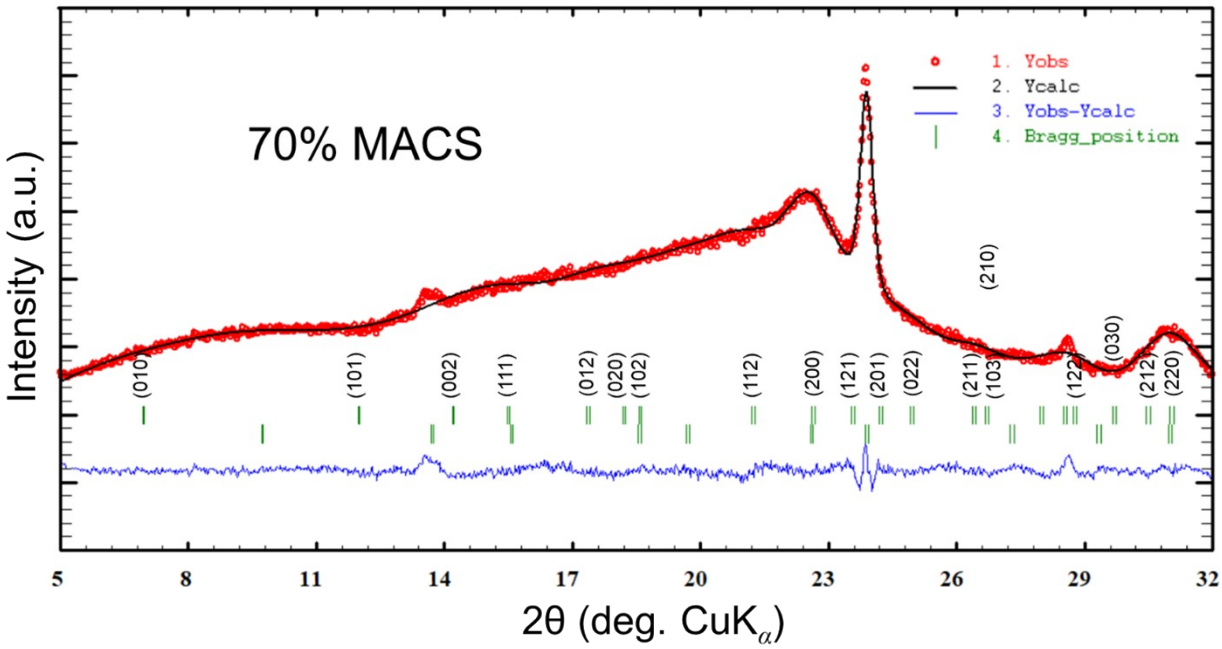

Figure S9. Rietveld refinement of XRD patterns PANI:CSA/MACS ($x \approx 60\%$) nanocomposites.

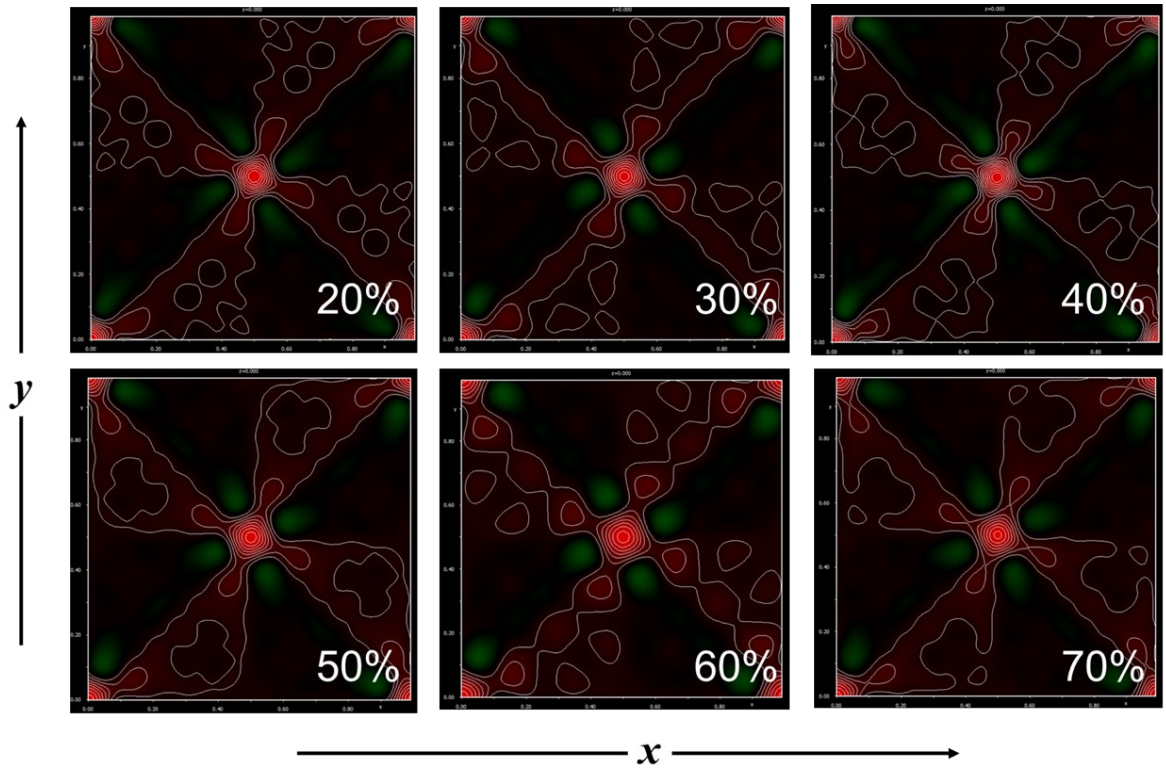

Figure S10. $F_o - F_c$ difference electron density map for α-MgAgSb.

S3. XPS Chemical States Details.

Table S2. Comparison of N 1s and C 1s deconvoluted components obtained from XPS for PANI:CSA and PMACS70 films. Binding-energy (B.E.) shifts (ΔB.E.) indicate electronic-structure modification upon filler incorporation, while variations in relative concentration ($\Delta_{Conc.}$) reflect changes in protonation level, polaron/bipolaron ratio, and interfacial interactions.

N 1s deconvoluted peaks	B.E. (eV) (PANI:CSA→ PMACS70)	$\Delta_{B.E}$ (eV)	Conc. (%) (PANI:CSA→ PMACS70)	$\Delta_{Conc.}$ (%)
-N= (imine Nitrogen)	399.1 → 399.3	+0.2	48.48 → 66.52	-18.04
-NH- (amine Nitrogen)	400.2 → 400.2	0	31.14 → 26.04	5.1
Polaron	401.6 → 401.3	-0.3	15.10 → 2.18	12.92
Bipolaron	403.4 → 402.5	-0.9	5.27 → 5.26	0.01
C 1s deconvoluted peaks				
C-C	284.3 → 284.2	0.1	62.33 → 31.62	30.71
C-N	285.3 → 284.8	0.5	25.92 → 38.03	-12.11
C-O	286.7 → 285.6	1.1	8.60 → 25.27	-16.67
C=O	287.9 → 286.7	1.2	3.15 → 5.08	-1.93

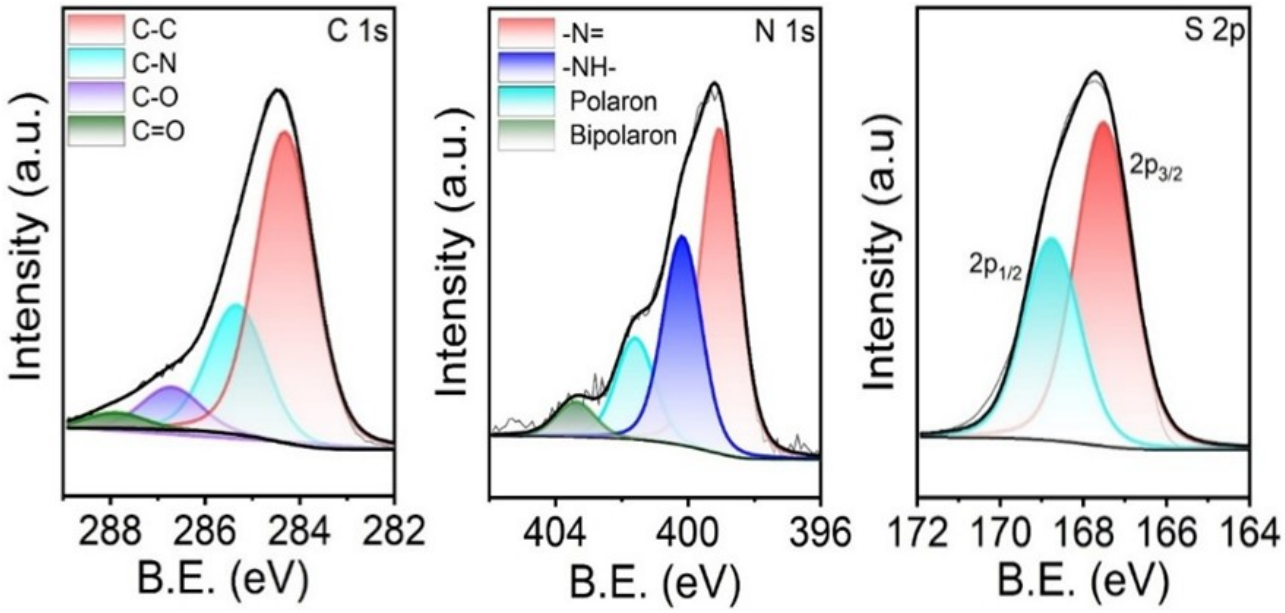

Figure S11. XPS wide-scan survey spectra and high-resolution elemental spectra for PANI:CSA

S4. Thermoelectric Properties and Mechanical Flexibility Testing.

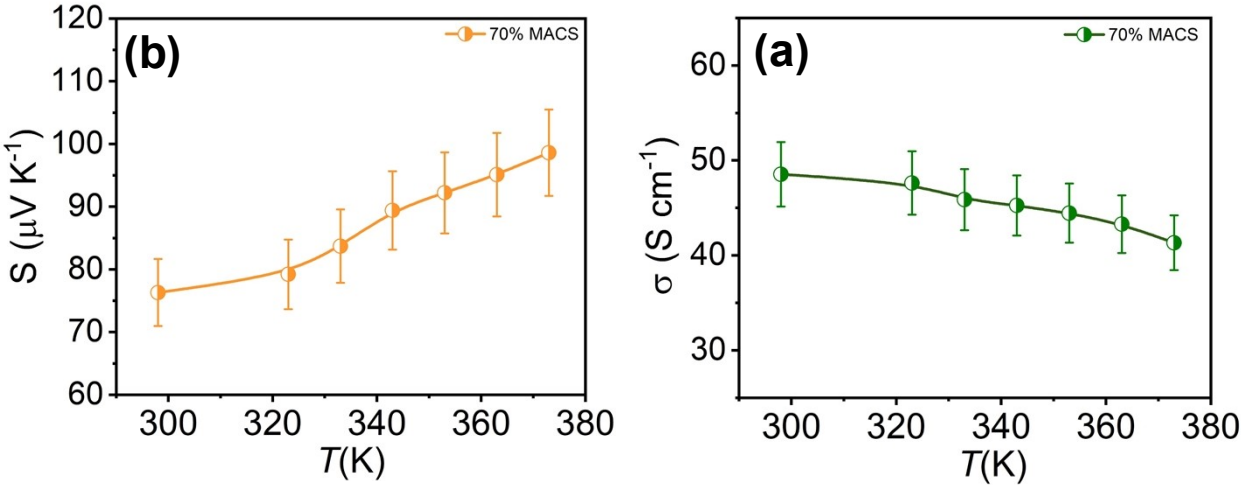

Figure S12. Temperature-dependent (a) electrical conductivity σ(T) and (b) Seebeck coefficient S(T) of the PMACS70 composite. Error bars represent the standard deviation obtained from PMACS70 flexible film, confirming the reproducibility and statistical reliability of the thermoelectric measurements.

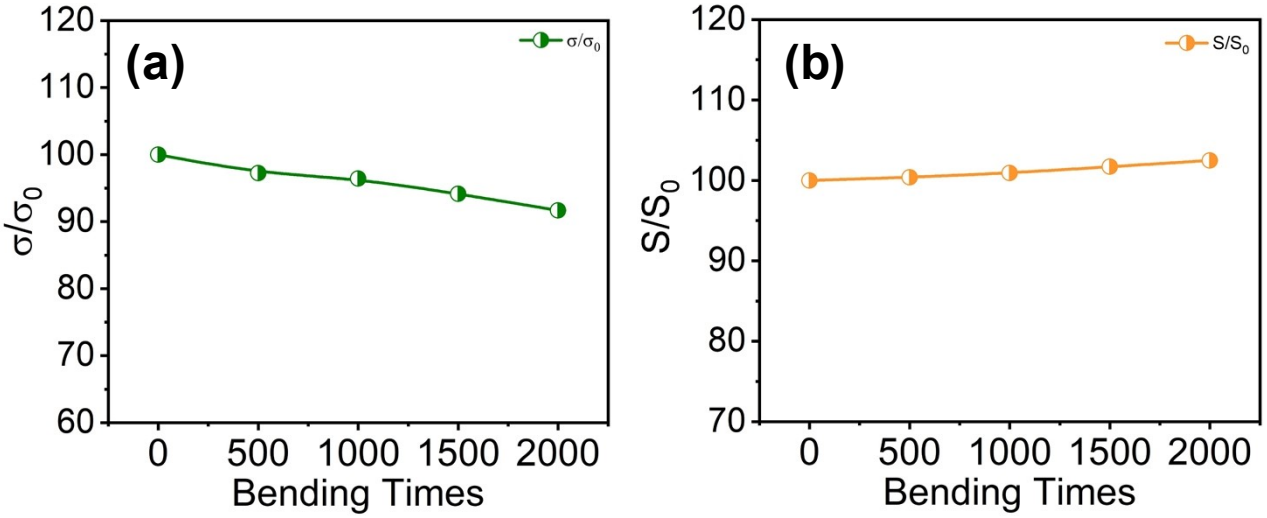

Figure S13. Mechanical flexibility and stability of the PMACS70 composite under repeated bending. (a) Normalized electrical conductivity (σ/σ_0) and (b) normalized Seebeck coefficient (S/S_0) as a function of bending cycles (0–2000)

S5. Comparison with State-of-the-Art PANI-Based Thermoelectric Composites

Table S3 summarizes representative literature reports of high-performance PANI-based thermoelectric composites. Table S3. Comparison of Thermoelectric performance in various PANI-based literatures.

Material Composite	σ $(S\,cm^{-1})$	S $(\mu V\,K^{-1})$	PF $(\mu W\,m^{-1}\,K^{-1})$	k $(W\,m^{-1}\,K^{-1})$	zT	**Ref.**
PANI-CSA/SWCNTs	769	65	176	0.43	0.12	[3]
PANI-CSA/DWCNT	610	61	220			[4]
PANI-HCl/SWCNTs	125	40	20	1.5	0.004	[5]
PANI/PPy/GNs	500	32.4	52.5			[6]
PANI/Te-NR	101	102	105	0.2	0.156	[7]
PANI/Bi_2S_3 NR	0.4	-42.8	0.07			[8]
PANI/MWCNTs/Te NR	137	63	54.4			[9]
PANI/SWCNTs/Te	345	54	101	0.2 – 0.4		[10]
PANI/$CuSbSe_2$/MWCNTs	21	-23.5	1.16	0.37 – 0.4	0.00002 – 0.0008	[11]
PANI/ZnSb	40	50	10			[12]
PANI/MACS (RT)	~49	~76	~28	~0.06	~0.13	This work
PANI/MACS (373 K)	~41	~99	40			This work

S6. Thermal Characterizations.

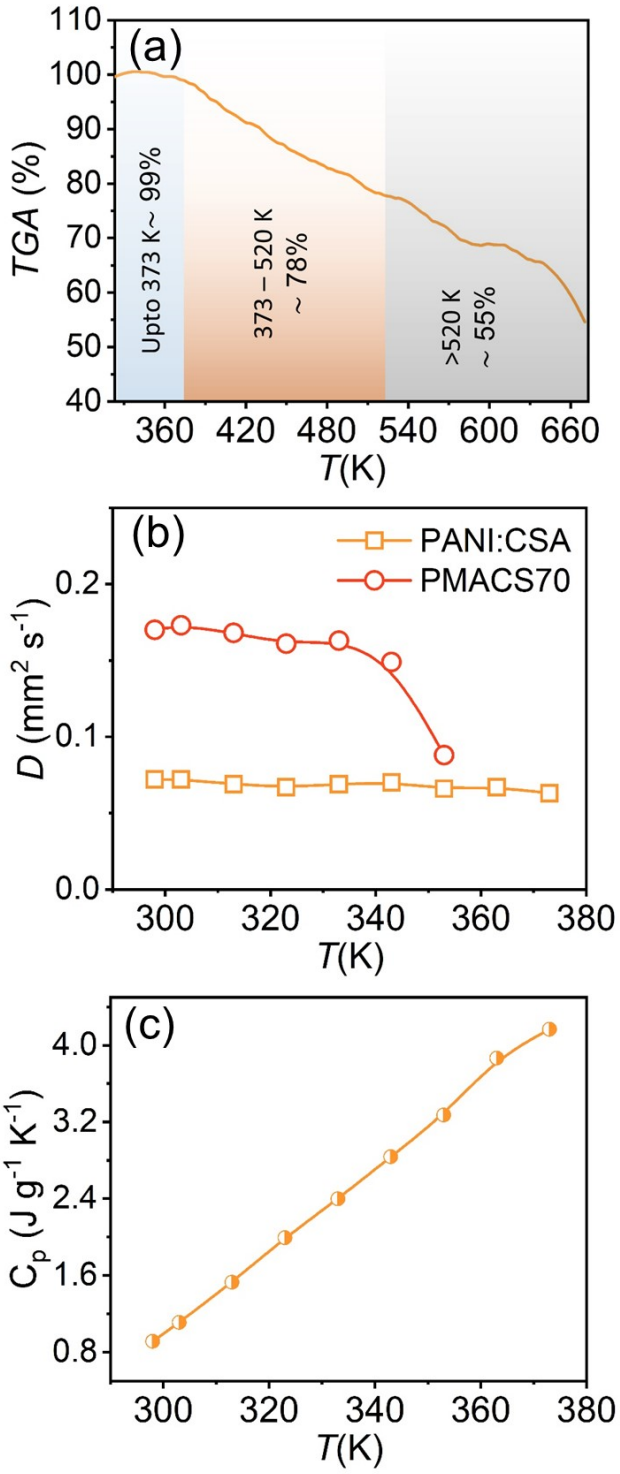

Figure S14. (a) TGA curve of PMACS70 showing its thermal stability, (b) Thermal diffusivity (D) for PANI:CSA and PMACS70 nanocomposite, (c) Heat Capacity for PMACS70 nanocomposite sample.

The TGA profile of PMACS70 as shown in Figure 14(a) exhibits the characteristic two-stage decomposition of free-standing PMACS70 film. Up to 373 K, negligible mass loss (~99 %) is observed, consistent with the literature reports attributing this region solely to moisture and residual *m*-cresol desorption.[13–16] Between 373 – 520 K, a gradual mass decrease to ~ 78% corresponds to the canonical first decomposition stage of PANI:CSA, involving CSA dopant evaporation, release of trapped m-cresol, and partial ES to EB deprotonation. Above ~520 K, continued mass loss arises from oxidative degradation of the polyaniline backbone. The final residue of ~55 – 60% at 660 – 670 K is substantially higher than that of neat PANI:CSA (~35 – 40%) due to thermally stable MACS filler.[13–16] Overall, PMACS70 retains the intrinsic decomposition sequence of PANI:CSA while exhibiting high – temperature structural robustness arising from its inorganic framework. So, the PMACS70 sample is thermally stable up to 373 K, the maximum temperature of our thermo-electric measurements. Figure 14(b) shows the diffusivity of PANI:CSA and PMACS70 samples. The diffusivity of the PMACS70 is almost linear in the range ~ 0.07 – 0.06 $mm^2\ s^{-1}$, while the diffusivity for PANI:CSA is stable upto 343 K, and then drops, which may be due to the wrapping up of the PANI:CSA films after 343 K. This suggests the good mechanical stability of PMACS70 as compared to PANI:CSA. Figure (c) shows the heat capacity (C_p) for PMACS70 film, which increases with temperature and reaches up to 4 J $g^{-1}\ K^{-1}$.

S7. Transport Modelling.

S7.1. Variable-Range Hopping and Charge-Localization Behavior. We modeled $\sigma(T)$ using Efros-Shklovskii variable-range hopping (ES-VRH), appropriate when a coulomb gap in the DOS due to electron–electron interactions [22] :

$$\sigma(T) = \sigma_0 \, exp\left[-\left(\frac{T_{ES}}{T}\right)^{\frac{1}{2}} \right]$$

Where T_{ES} is Efros–Shklovskii characteristic temperature, and σ_0 is the pre-exponential factor.

$$T_{ES} = \frac{\beta e^2}{4\pi\varepsilon_0\varepsilon_r k_B \xi}$$

Where β, e, ε_0, ε_r, k_B represents numerical constant (≈ 2.8), elementary charge (1.602×10^{-19} C), vacuum permittivity (8.854×10^{-12} F/m), relative dielectric constant of the material, and Boltzmann constant (1.381×10^{-23} J/K). T_{ES} is a signature of Coulomb interaction–dominated hopping and links electrical conductivity, dielectric screening, and localization length (ξ). T_{ES} is inversely proportional to ξ, and can be used to extract localization length from transport data. In the Mott-VRH regime, a constant density of states (DOS) near the Fermi level is assumed, where $\sigma(T)$ follows the relation

$$\sigma(T) = \sigma_0 \, exp\left[-\left(\frac{T_0}{T}\right)^{\frac{1}{4}} \right]$$

In ES–VRH theory, the localization length ξ represents the decay length of the electronic wavefunction; therefore, a larger ξ corresponds to less localized and more extended hopping states. ξ should thus be interpreted as the mesoscopic hopping radius in the composite, rather than the microscopic localization of individual polarons on the PANI chain. Extracting T_{ES} from our experimental fits provides direct insight into the electronic disorder and carrier confinement in conducting polymer composites. Figure S16 ($\ln \sigma vs$ ($-T^{-1/2}$)) shows excellent linearity for every composition over ~300 – 380 K. The slope magnitude (T_{ES}) decreases (from ~7700 to 600 K) while the ES pre-factor σ_0 increases with MACS filler (from ~1.8 – 12 S cm^{-1}). Through

$T_{ES} \propto e^2/(\varepsilon\varepsilon_0 k_\beta \xi)$, this indicates a progressive increase of the localization length ξ as MACS content rises as shown in Figure S17 (values compiled in Table S4 taking ε in a wide range). The observed increase in ξ with MACS loading therefore reflects a more interconnected, dielectric-screened hopping network formed by PANI-coated MACS grains, enabling carriers to hop over longer distances. This mesoscopic extension coexists with *microscopic* polaron localization on PANI segments, evidenced independently by XPS, Raman, and UV–Vis and corresponds to a weaker Coulomb-gap constraint on mesoscopic hopping MACS-rich films, even though the microscopic polaron states becomes more localized along the PANI backbone[19–22].

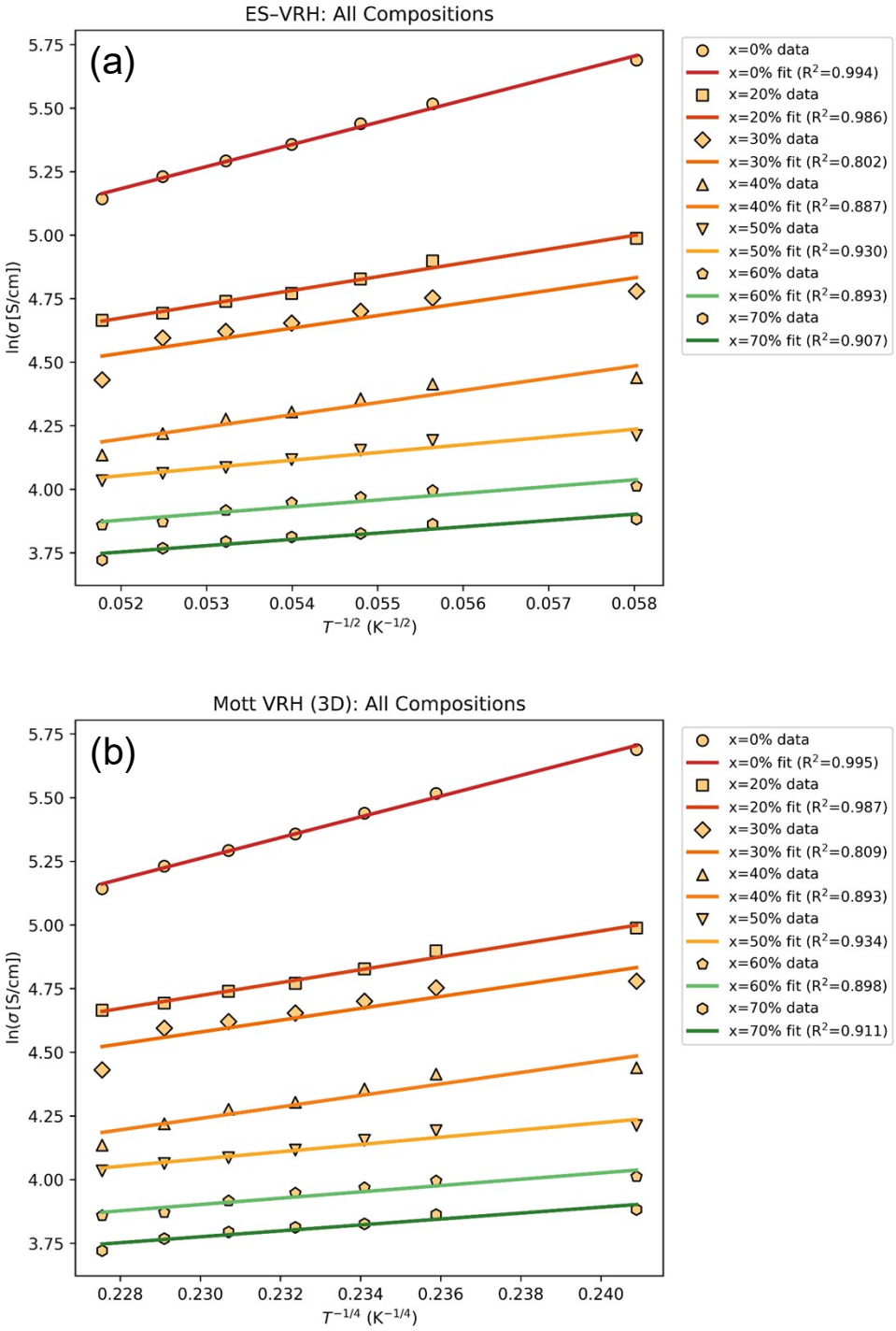

Figure S15. Variable-range hopping analysis for PMACS composites. (a) Efros–Shklovskii (ES) and (b) Mott 3D VRH fits of ln σ vs $T^{-1/2}$ and $T^{-1/4}$ for x = 0–70 wt % films, respectively.

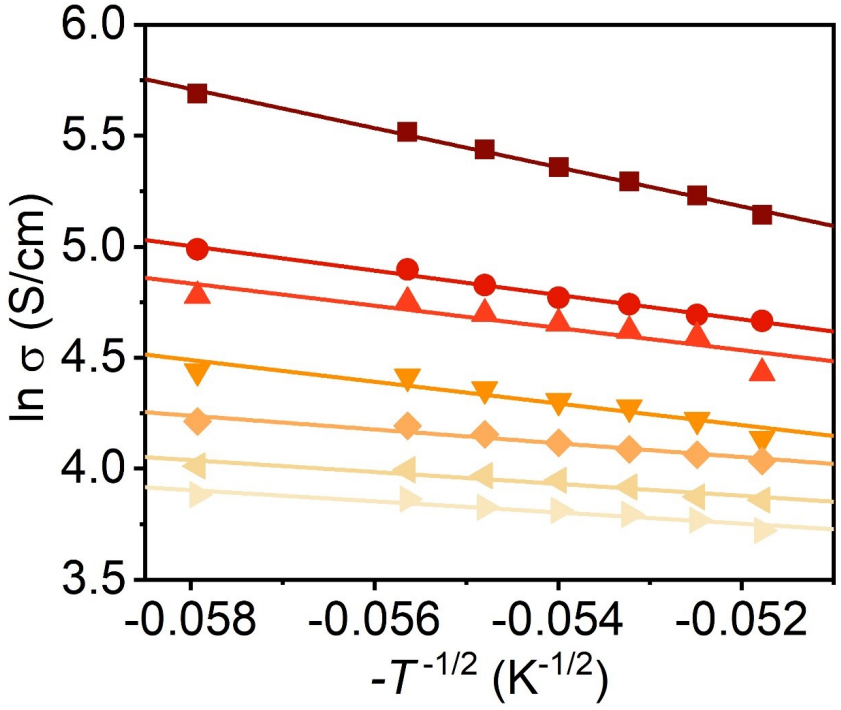

Figure S16. Temperature dependent ES-VRH model fitting of electrical conductivity with a temperature exponent of 1/2, demonstrating linear behavior.

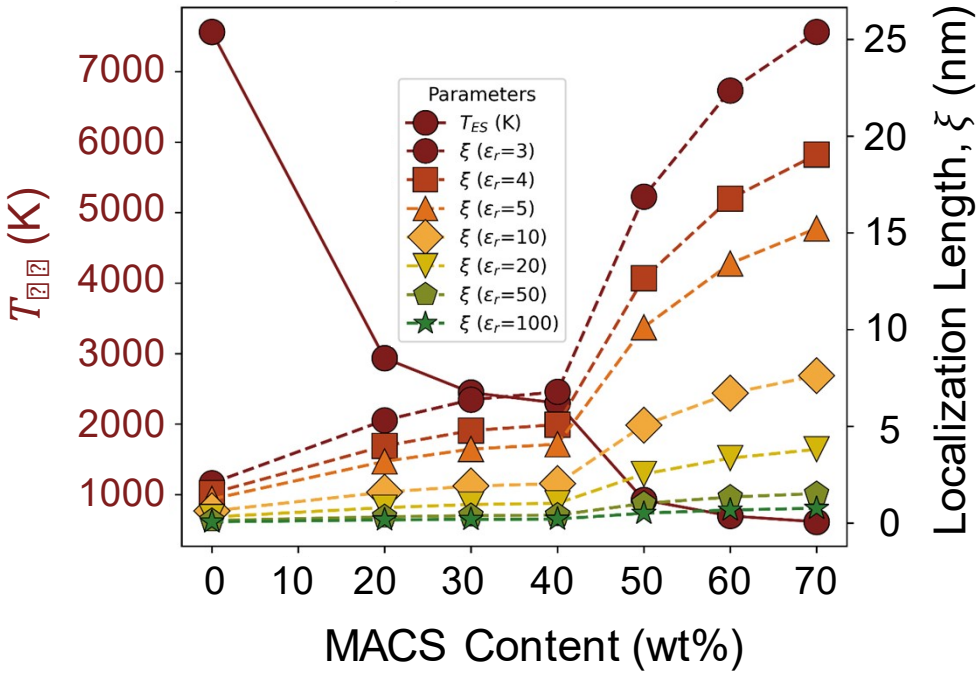

Figure S17. Characteristic temperature (T_{es}) and localization length (ξ) as a function of MACS loading (0–70 wt %).

Table S4. Localization Length (ξ) as a function of dielectric constant (ε) for PANI/MACS composites with varying filler content.

MACS wt.%	$\varepsilon = 3$	$\varepsilon = 5$	$\varepsilon = 10$	$\varepsilon = 20$	$\varepsilon = 50$	$\varepsilon = 100$
0	2.0	1.20	0.601	0.300	0.120	0.060
20	5.16	3.10	1.55	0.775	0.310	0.155
30	6.22	3.73	1.87	0.934	0.373	0.187
40	6.53	3.92	1.96	0.982	0.392	0.196
50	16.16	9.70	4.85	2.42	0.970	0.485
60	21.78	13.07	6.53	3.27	1.307	0.653
70	24.56	14.74	7.37	3.68	1.474	0.737

S7.2. Kang–Snyder Transport Modeling. The Kang–Snyder framework expresses thermoelectric transport in terms of a transport edge E_t and a scattering parameter *s*. The measurable properties follow from a transport kernel $\sigma_E(E,T) = \sigma_{E0}(T)\left(\frac{E - E_t}{k_B T}\right)^s$ for $E \geq E_t$, integrated against the Fermi window, which yields

$\sigma = \sigma_{E0}(T)\, s\, F_{s-1}(\eta)$

$$S = \frac{k_B}{e}\left[\frac{(s+1)F_s(\eta)}{F_{s-1}(\eta)} - \eta\right]$$

where $F_j(\eta)$ is the complete Fermi integral of order j, k_B is Boltzmann's constant, e is the elementary charge, and $\eta = (E_F - E_t)/k_B T$ is the reduced chemical potential. For a fixed s, the Seebeck relation determines η uniquely; the conductivity then follows from a lateral shift set by transport coefficient, $\sigma_{E0}(T)$. This statistical-coefficient separation is the essence of Kang Snyder analysis: $S(\eta)$ encodes the statistics, while $\sigma_{E0}(T)$ contains morphology/percolation.

As shown in Figure S18(a), a plot of S vs σ at 297 K, the experimental $S(\sigma)$ loci are described by the $s = 1$, whereas $s = 2$ and $s = 3$ curves systematically miss the data at both high

and low S. The synthesized PMACS is therefore classified as an $s \approx 1$ conductor, indicating polymer-like scattering preserved over all MACS loadings. Figure 18(b) presents the Kang–Snyder $s \approx 1$ transport family at 297 K, where experimental $S - \sigma$ data align closely with the CT-model curves across increasing σ_{E0} values. The rightward shift with MACS content indicates enhanced percolative connectivity signifying improved interfacial connectivity across the hybrid network, consistent with polymer-like diffusive scattering retained over all compositions. The KS-transport model fits for PMACS composites at different temperatures has been shown in Figure 19(a – f). The reduced chemical potential (η) extracted from the Seebeck coefficient exhibits a systematic decrease both with increasing temperature and with increasing MACS content (Figure S20). At 297 K, η drops from $\approx$ 31 for pristine PANI:CSA to $\approx$ 3.5 for the MACS 70 wt % composite, while further heating leads to a gradual decline across all compositions. This monotonic reduction in η signifies a progressive lowering of carrier concentration and a shift of the Fermi level away from the transport edge as inorganic content increases. Such behavior reflects partial deprotonation of PANI chains and charge localization induced by the semiconducting MACS phase, in accordance with the Raman and XPS signatures of reduced polarons density.

The temperature dependence of the transport coefficient follows the percolative Kang-Snyder relation

$$\sigma_{E0} \propto exp\left[-\left(\frac{W^{1/2}}{k_B T}\right)^{1/2} \right]$$

where $W^{1/2}$ represents an effective disorder-related energy barrier. As shown in Figure S21, Linear fits of $\ln \sigma_{E0}$ versus $(1/T)^{1/2}$ yield $W^{1/2}$ values near zero for pristine PANI, rising to ~ 0.05–0.06 eV for 20–30 wt % MACS, falling again near 40 wt %, and peaking around ~ 0.13–0.14 eV for 60 wt %, followed by a slight decrease at 70 wt %. This non-monotonic evolution delineates three regimes: (i) a strongly connected polymeric network at low loading, (ii) increased structural

disorder and interfacial scattering near intermediate loading, and (iii) partial re-establishment of connectivity at high loading. The KS model thus quantitatively describes the thermoelectric transport within a unified scattering class, linking the decrease in carrier concentration ($\eta\downarrow$) and enhancement in connectivity ($\sigma_{E0}\uparrow$) to the composite microstructure.

The Kang–Snyder (KS) framework[23] effectively captures the overall $S-\sigma$ correlations and confirms an invariant scattering exponent $s=1$, however it fails to reproduce the systematic leftward shift observed for high-MACS compositions in the charge-transport (CT) family curves.[24] Even after adjusting the reduced conductivity transport coefficient σ_{E0}, the data for MACS-rich composites (≥ 50 wt %) consistently lie at lower σ values than the corresponding KS-predicted isotherms. This deviation signifies an additional conductivity suppression mechanism that does not alter the Seebeck statistics and hence cannot be explained by carrier-statistics modulation or morphological percolation alone. In essence, the SLoT model[25] retains the statistical foundation of KS transport but introduces an energetic descriptor for localization as described in section S3.3 below. Within this dual framework, low-MACS films are governed by delocalized diffusive transport (small W_H), whereas high-MACS composites operate in a semi-localized regime where localized barriers regulate conductivity without compromising the Seebeck coefficient. The resulting balance between connectivity enhancement (σ_{E0}) and localization penalty (W_H) explains the experimentally observed leftward deviation in the CT-family curves and the optimized thermoelectric response at intermediate MACS concentrations.

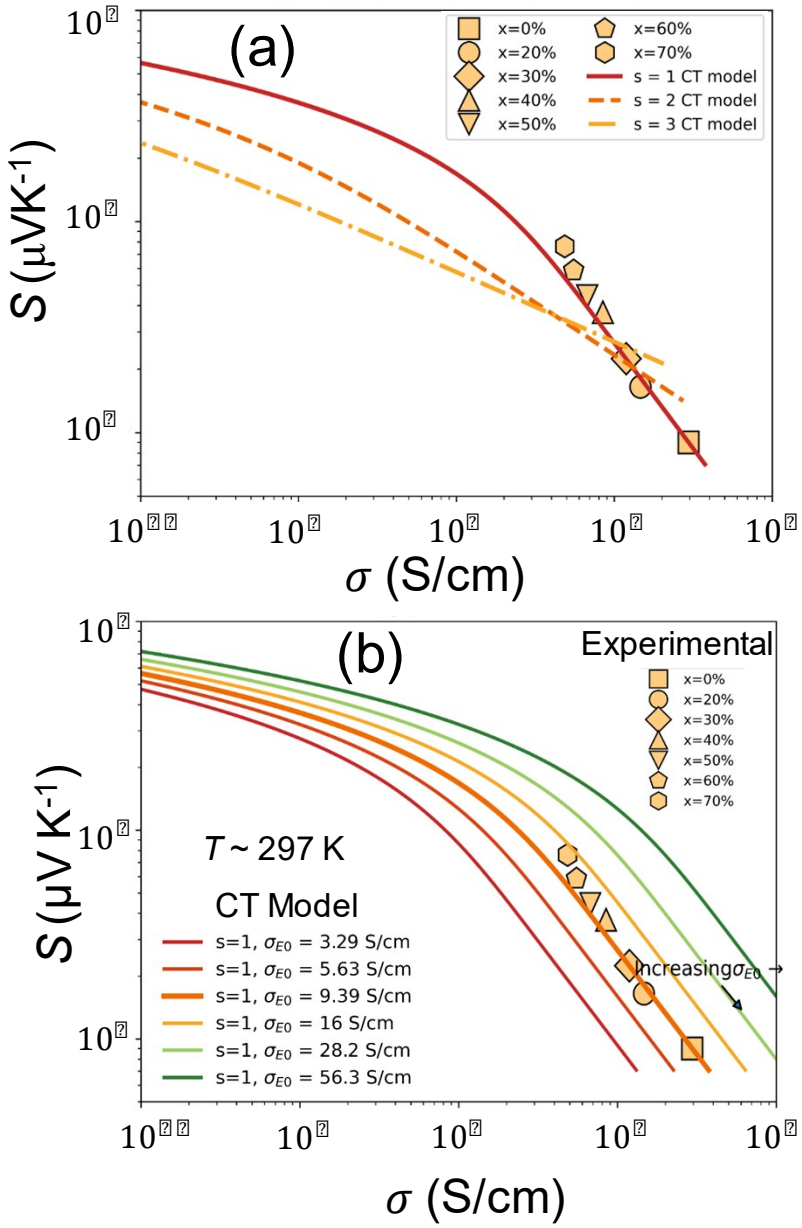

Figure S18. (a) Kang–Snyder charge transport model fits at T ~ 297 K with different energy-dependent scattering exponents (*s*), as described in the main text. (b) The experimental data at 297 K, align with the *s* = 1 curve with increasing transport coefficients.

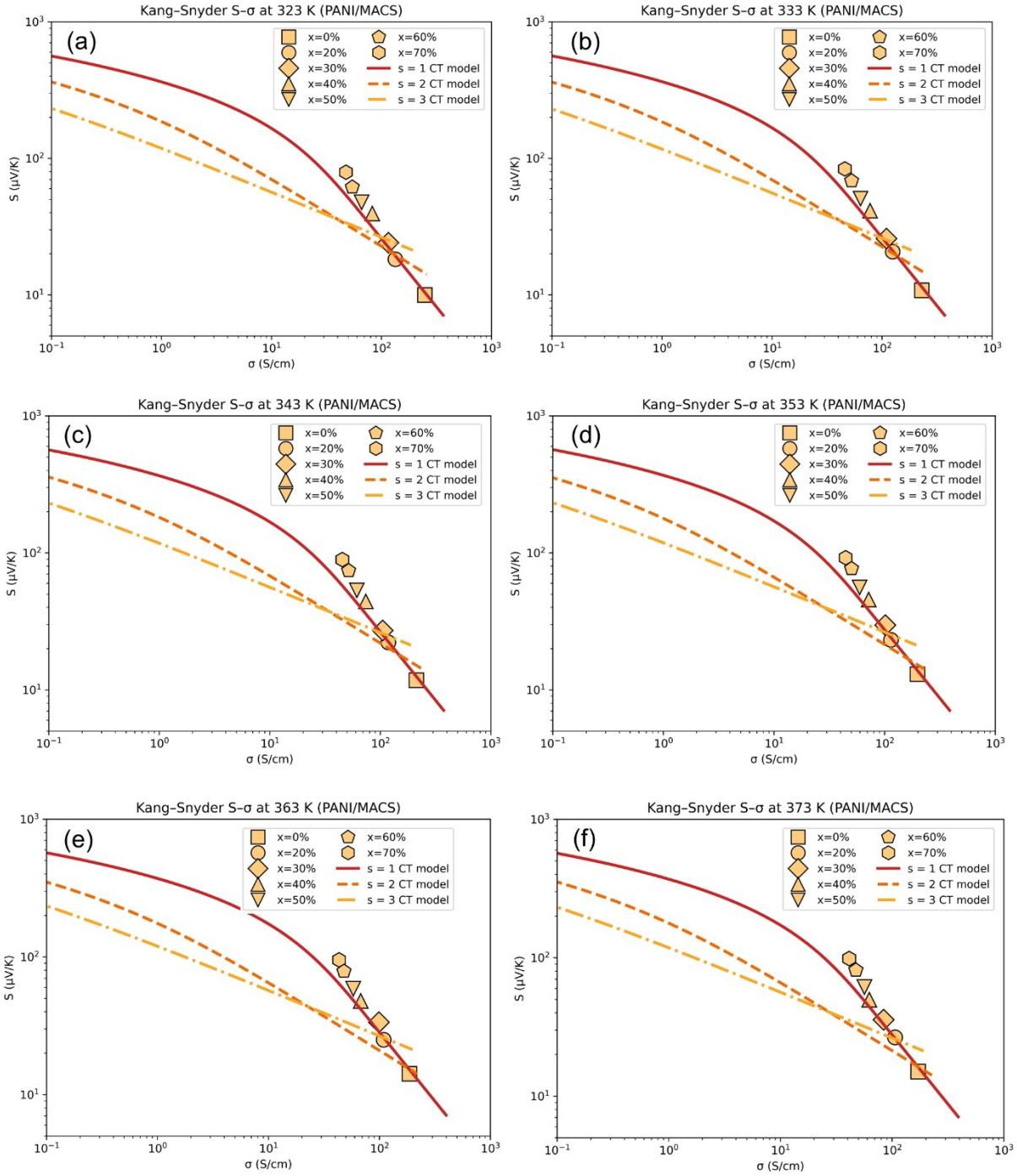

Figure S19. Kang–Snyder transport model fits for PANI:CSA/MACS composites at different temperatures. Experimental Seebeck coefficient (S) versus electrical conductivity (σ) relationships for compositions *x = 0–70 wt %* at (a) 323 K, (b) 333 K, (c) 343 K, (d) 353 K, (e) 363 K, and (f) 373 K. Solid, dashed, and dash-dot lines represent Kang–Snyder (CT) model calculations with scattering exponents *s = 1, 2,* and *3,* respectively. All datasets collapse along the *s = 1* curve, confirming polymer-like diffusive scattering preserved across all MACS loadings. Deviations at high filler contents reflect conductivity suppression due to interfacial localization and energy-filtering effects

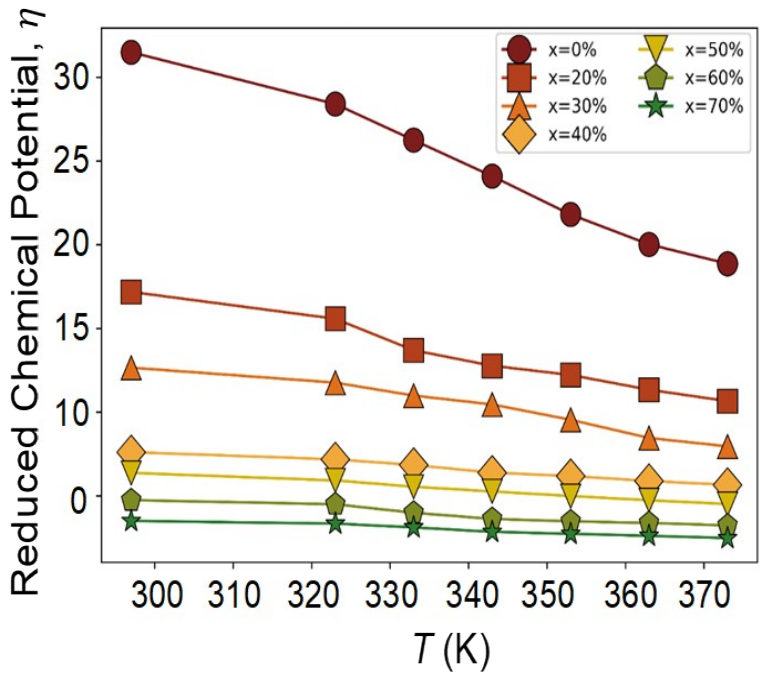

Figure S20. Reduced chemical potential decreasing as a function of both increasing temperature and MACS content representing reduced doping level.

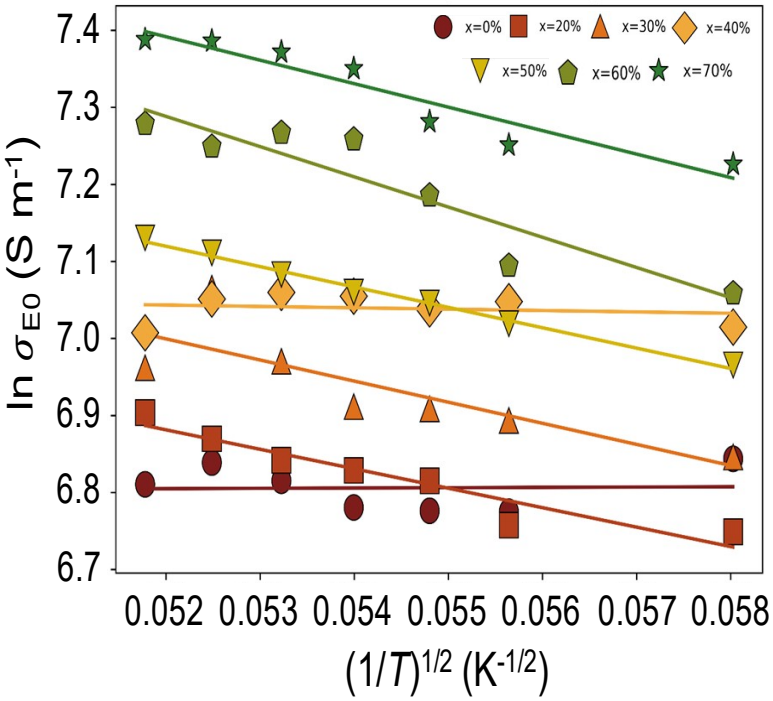

Figure S21. Temperature dependence of reduced conductivity transport coefficient (ln σ_{E0}) for PANI:CSA/MACS composites extracted from Kang–Snyder analysis

S7.3. Semi-Localized Transport (SLoT) analysis. To account for this behavior, the semi-localized transport (SLoT) model extends the KS formalism by incorporating the effect of spatial carrier localization into the transport coefficient. In this framework, energy-dependent conductivity becomes

$$\sigma_E(E,T) = \sigma_0 exp\left(-\frac{W_H}{k_B T}\right)\left(\frac{E-E_t}{k_B T}\right)^s, (E \geq E_t)$$

where the additional term from Kang-Snyder model is the energy-independent transport function term $\sigma_{E0}(T,c) = \sigma_0\, exp\left(-\frac{W_H(c)}{k_B T}\right)$, describing hopping-like transport behavior, leading to macroscopic relations.

$$\sigma(T,\eta) = \sigma_0\, s\, F_{s-1}(\eta) exp\left(-\frac{W_H}{k_B T}\right),$$

$$S = \frac{k_B}{e}\left[\frac{(s+1)F_s(\eta)}{sF_{s-1}(\eta)} - \eta\right]$$

Here, σ_0 is the delocalized limit of the transport coefficient, W_H represents the localization energy associated with hopping across spatially confined states or interfacial potential barriers, c represents the carrier concentration, and $F_j(\eta)$ is the Fermi integral of order j. Because the Seebeck coefficient depends solely on η and s, the inclusion of W_H exponentially suppresses conductivity while leaving $S(\eta)$ unchanged, precisely reproducing the leftward displacement of the experimental data relative to the KS prediction. The exponential damping factor $exp(-W_H/k_B T)$ bridges the gap between delocalized and hopping regimes, enabling a quantitative description of systems where interfacial heterogeneity and disorder coexist with moderate carrier delocalization. Experimentally, the degree of localization can be quantified by analyzing the Arrhenius-type temperature dependence of the reduced conductivity transport coefficient:

$$ln\ \sigma_{E0} = \ln \sigma_0 - \frac{W_H}{k_B T}$$

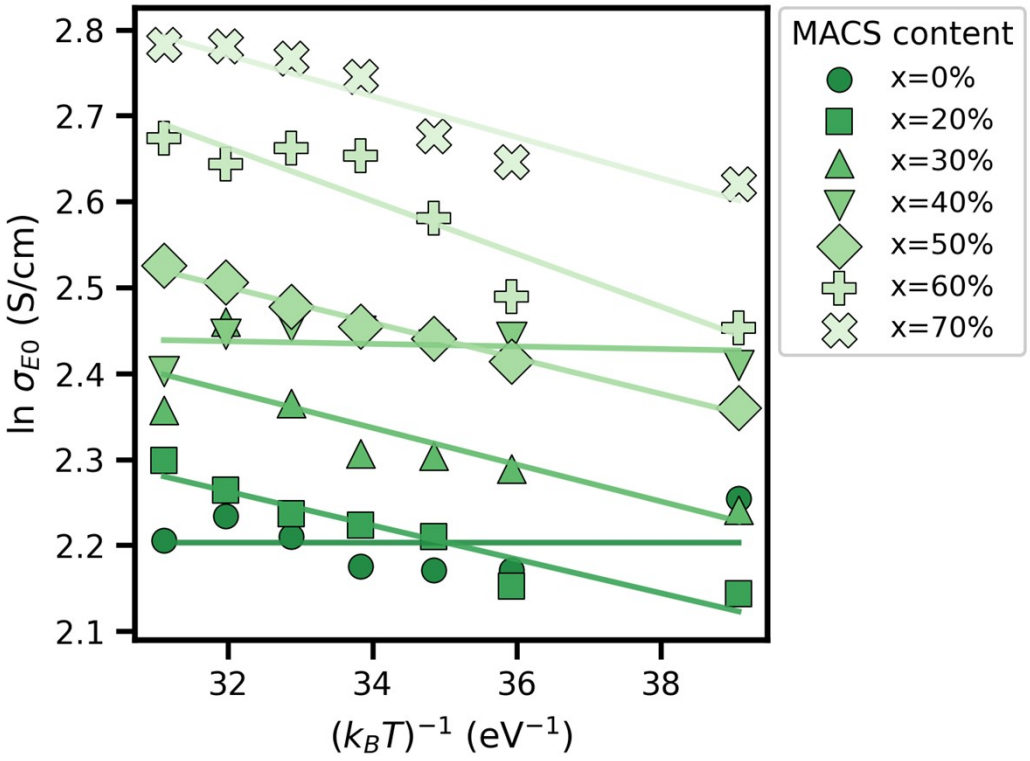

Figure S22. Arrhenius-type temperature dependence of reduced conductivity transport coefficient ($\ln \sigma_{E0}$) from SLoT analysis for PANI:CSA/MACS composites.

References.

[1] Z. Liu, N. Sato, W. Gao, K. Yubuta, N. Kawamoto, M. Mitome, K. Kurashima, Y. Owada, K. Nagase, C.-H. Lee, J. Yi, K. Tsuchiya, T. Mori, *Joule* **2021**, *5*, 1196.

[2] J. P. Pouget, M. E. Jozefowicz, A. J. Epstein, X. Tang, A. G. MacDiarmid, *Macromolecules* **1991**, *24*, 779.

[3] Q. Yao, Q. Wang, L. Wang, L. Chen, *Energy Environ. Sci.* **2014**, *7*, 3801.

[4] H. Wang, S. Yi, X. Pu, C. Yu, *ACS Appl. Mater. Interfaces* **2015**, *7*, 9589.

[5] Q. Yao, L. Chen, W. Zhang, S. Liufu, X. Chen, *ACS Nano* **2010**, *4*, 2445.

[6] Y. Wang, J. Yang, L. Wang, K. Du, Q. Yin, Q. Yin, *ACS Appl. Mater. Interfaces* **2017**, *9*, 20124.

[7] Y. Wang, S. M. Zhang, Y. Deng, *J. Mater. Chem. A* **2016**, *4*, 3554.

[8] Y. Wang, G. Liu, M. Sheng, C. Yu, Y. Deng, *J. Mater. Chem. A* **2019**, *7*, 1718.

[9] Y. Wang, C. Yu, M. Sheng, S. Song, Y. Deng, *Adv Materials Inter* **2018**, *5*, 1701168.

[10] L. Wang, Q. Yao, W. Shi, S. Qu, L. Chen, *Mater. Chem. Front.* **2017**, *1*, 741.

[11] A. S. Kshirsagar, P. V. More, A. Dey, P. K. Khanna, *Dalton Trans.* **2019**, *48*, 14497.

[12] A. Sharma, N. S. Chauhan, M. Nishimagi, T. Mori, *Materials Today Physics* **2025**, *57*, 101794.

[13] V. J. Babu, S. Vempati, S. Ramakrishna, *MSA* **2013**, *04*, 1.
[14] D. Yalcin, S. Bamford, M. Espiritu, N. Rigopoulos, I. Martinez-Botella, D. Alexander, Y. Gozukara, M. Greaves, E. A. Bruton, P. J. Kinlen, S. Howard, P. J. Pigram, B. W. Muir, T. M. Kohl, *Polymer Degradation and Stability* **2023**, *215*, 110427.
[15] W. Li, M. Wan, *J. Appl. Polym. Sci.* **1999**, *71*, 615.
[16] O. Abdulrazzaq, S. E. Bourdo, V. Saini, F. Watanabe, B. Barnes, A. Ghosh, A. S. Biris, *RSC Adv.* **2015**, *5*, 33.
[17] A. L. Efros, M. Pollak, in *March 1*, De Gruyter, **1986**, pp. 497–498.
[18] S. Shekhar, V. Prasad, S. V. Subramanyam, *Physics Letters A* **2006**, *360*, 390.
[19] N. Papadopoulos, G. A. Steele, H. S. J. Van Der Zant, *Phys. Rev. B* **2017**, *96*, 235436.
[20] A. J. Epstein, W.-P. Lee, V. N. Prigodin, *Synthetic Metals* **2001**, *117*, 9.
[21] M. Baćani, M. Novak, I. Kokanović, D. Babić, *Synthetic Metals* **2013**, *172*, 28.
[22] A. L. Efros, B. I. Shklovskii, *J. Phys. C: Solid State Phys.* **1975**, *8*, L49.
[23] S. D. Kang, G. J. Snyder, *Nature materials* **2017**, *16*, 252.
[24] P. Kumar, E. W. Zaia, E. Yildirim, D. M. Repaka, S.-W. Yang, J. J. Urban, K. Hippalgaonkar, *Nature communications* **2018**, *9*, 5347.
[25] S. A. Gregory, R. Hanus, A. Atassi, J. M. Rinehart, J. P. Wooding, A. K. Menon, M. D. Losego, G. J. Snyder, S. K. Yee, *Nature materials* **2021**, *20*, 1414.